

# Higher rank chirality and non-Hermitian skin effect in a topoelectrical circuit

Penghao Zhu<sup>1</sup>, Xiao-Qi Sun<sup>1</sup>,  
Taylor L. Hughes<sup>1\*</sup>, and Gaurav Bahl<sup>2\*</sup>

<sup>1</sup>Department of Physics and Institute for Condensed Matter Theory

<sup>2</sup>Department of Mechanical Science and Engineering,, University of Illinois  
Urbana-Champaign, Urbana, Illinois 61801, USA

\*To whom correspondence should be addressed: hughest@illinois.edu, bahl@illinois.edu

July 7, 2022

## Abstract

While chirality imbalances are forbidden in conventional lattice systems, non-Hermiticity can effectively avoid the chiral-doubling theorem to facilitate 1D chiral dynamics. Indeed, such systems support unbalanced unidirectional flows that can lead to the localization of an extensive number of states at the boundary, known as the non-Hermitian skin effect (NHSE). Recently, a generalized (rank-2) chirality describing a 2D robust gapless mode with dispersion  $\omega = k_x k_y$  has been introduced in crystalline systems. Here we demonstrate that rank-2 chirality imbalances can be established in a non-Hermitian (NH) lattice system leading to momentum-resolved chiral dynamics, and a rank-2 NHSE where there are both edge- and corner-localized skin modes. We then experimentally test this phenomenology in a 2-dimensional topoelectric circuit that implements a NH Hamiltonian with a long-lived rank-2 chiral mode. Using impedance measurements, we confirm the rank-2 NHSE in this system, and its manifestation in the predicted skin modes and a highly unusual momentum-position locking response. Our investigation demonstrates a circuit-based path to exploring higher-rank chiral physics, with potential applications in systems where momentum resolution is necessary, e.g., in beamformers and non-reciprocal devices.

Chirality is a key characteristic of robust gapless modes – only by coupling a set of such modes with vanishing net chirality can we destabilize the modes and open an energy gap. For example, a 1D chiral mode is a one-way conducting channel with a linear dispersion  $\omega = vk$ . Its chirality is intrinsically defined as the sign of its group velocity  $v$  without requiring any other constraints. To open a gap in a chiral channel one needs to backscatter and reverse the current

flow, which can be accomplished only by coupling two such modes that have opposite group velocity/chirality. This robustness is heralded by the so-called chiral anomaly: subjecting a chiral channel to an electric field generates extra charges that break the conservation of the electric charge current by an amount proportional to the net chirality.

With crystalline symmetries, one can generalize the concept of chirality, robustness, and anomalies for gapless modes with more complex dispersion. Indeed, a generalized chirality for gapless modes with dispersion  $\omega \sim k_x k_y$  has been recently proposed in mirror symmetric systems<sup>1</sup>. Such a chiral mode has a non-conserved momentum current (momentum anomaly) in response to an electric field, and has a non-conserved charge current (charge anomaly) in response to a strain field. Since the charge anomaly is induced by a rank-2 (two-index) tensor gauge field (the strain tensor), this generalized chiral mode has been dubbed a rank-2 chiral mode. In contrast, the usual 1D chiral mode is anomalous in the presence of a rank-1 (vector) gauge field, and we therefore refer to it as a rank-1 chiral mode.

Although isolated chiral modes widely exist in the band structures of lattice systems, there is a no-go theorem excluding the lattice realization of a nonzero *net* chirality<sup>2,3</sup>. However, one can avoid the no-go theorem and observe unusual chiral dynamics on boundaries of topological phases<sup>4</sup>, in periodically-driven Floquet systems<sup>5</sup>, or in non-Hermitian (NH) systems<sup>6-8</sup>. In the latter case, which is our focus, one can apply appropriate gain and loss to a lattice system that will effectively generate a chirality imbalance. Unidirectional flows are established in the long-time dynamics of such systems<sup>9,10</sup>, and these lead to the localization of an extensive number of states at the boundary; a phenomenon known as the non-Hermitian skin effect (NHSE)<sup>11-15</sup>. Heuristically, if there is a 1D chiral mode that is the most amplified (or least damped) in a NH system, then this mode is long-lived and can dominate the long time dynamics. Such a mode will produce a net 1D chirality and hence a unidirectional particle current that accumulates density on a boundary thus forming the NHSE.

Inspired by this remarkable effect, we will illustrate the novel long-time phenomenology of a NH system dominated by a nonzero rank-2 chirality. We demonstrate that the nonzero rank-2 chirality leads to an unconventional momentum resolved chiral dynamics. Such dynamics generate skin modes on the edges and corners of an open square system with locations determined by a combination of the rank-2 chirality and the momentum of the excitation. As a first experimental probe of the rank-2 chirality and its associated unconventional dynamics, we experimentally implement a NH lattice system with a long-lived rank-2 chiral mode (i.e., the rank-2 chiral mode has the slowest damping rate). Specifically, we implement a NH topoelectrical circuit<sup>16</sup> that hosts a rank-2 chiral mode, and we observe the predicted momentum resolved dynamics and the corresponding rank-2 NHSE.

A rank-2 chiral fermion mode in 2D has the dispersion<sup>1</sup>:

$$E(\mathbf{k}) = \hbar v \xi k_x k_y - \mu, \quad (1)$$

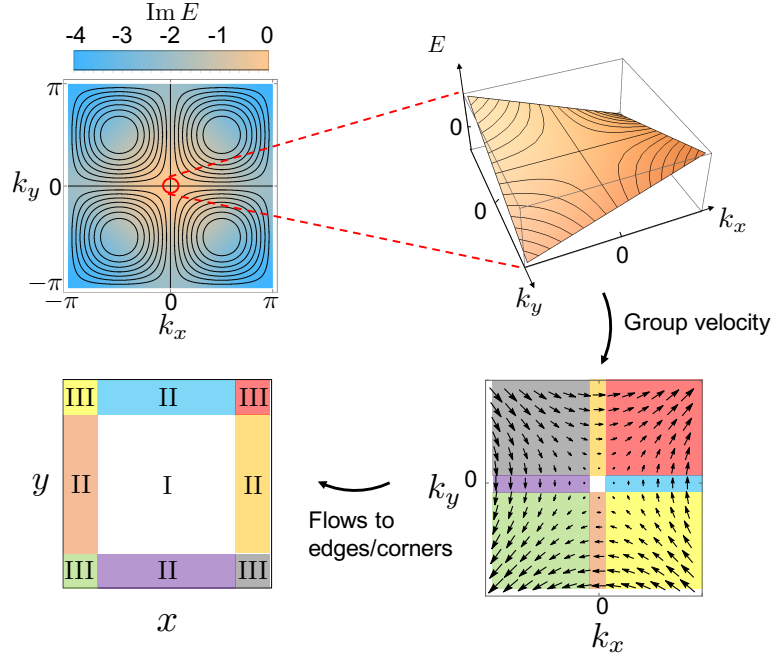


**Figure 1: Rank-2 chiral mode as a long-lived mode of a non-Hermitian lattice Hamiltonian and the resulting rank-2 NHSE.** The top left panel shows the isoenergy contours of  $\text{Re } E = \sin k_x \sin k_y$  (black lines) and the loss  $\text{Im } E = \cos k_x + \cos k_y - 2$ . The top right panel manifests the dispersion of long-lived rank-2 chiral mode around  $\Gamma = (0, 0)$ . The group velocity field of the long-lived rank-2 chiral mode around  $\Gamma = (0, 0)$  is shown in the bottom right panel. States with momenta in regions with different colors flow to different regions in spatial space, which leads to bulk-, edge-, and corner- localized modes as indicated in the bottom left panel.

where  $v$  is a (Fermi) velocity,  $\xi$  is a length scale, and  $\mu$  is the Fermi energy. The isoenergy contours and dispersion relation for Eq. 1 are shown in Fig. 1. Importantly, if we impose a mirror symmetry about the line  $x = y$  we can define a rank-2 chirality as  $\chi_2 \equiv \text{sgn}(v\xi)$ . Indeed, such a mirror symmetry guarantees that one cannot continuously deform  $k_x k_y \rightarrow -k_x k_y$  without breaking the symmetry, and hence  $\chi_2$  is a fixed, well-defined sign.

It is illustrative to regard the rank-2 chiral mode as a collection of 1D chiral modes with a nontrivial chirality pattern. In particular we can describe the rank-2 chiral mode as a family of 1D chiral modes along the  $x$ -direction ( $y$ -direction) parameterized by  $k_y$  ( $k_x$ ), having a set of 1D chiralities given by  $\chi_{1x}(k_y) = \chi_2 \text{sgn } k_y$  ( $\chi_{1y}(k_x) = \chi_2 \text{sgn } k_x$ ). With this understanding, the robustness and the associated anomalies of a rank-2 chiral mode can be straightforwardly derived from the properties of the 1D chiral modes. As mentioned, a 1D chiral mode with a positive (negative) chirality has an anomalous charge conservation law proportional to the (opposite of the) external electric field<sup>17</sup>.

For a uniform system the anomalous conservation law reduces to:

$$\partial_t \rho = \chi_1 \frac{e}{2\pi\hbar} E_x \quad (2)$$

where  $\rho$  is the charge density. For example, if we turn on an electric field  $E_x$  via the Faraday effect, e.g., by adiabatically shifting the  $x$ -component of the vector potential,  $A_x$ , by  $\hbar/eL$  where  $L$  is the linear size of the system along  $x$ , then  $\chi_1$  particles are generated. The rank-2 chiral mode is a collection of 1D chiral modes having momentum-dependent chiralities, though the net chiralities  $\chi_X = \sum_{k_y} \chi_{1x}(k_y)$ ,  $\chi_Y = \sum_{k_x} \chi_{1y}(k_x)$  in both directions vanish (as they must from time-reversal symmetry). As such a rank-2 chiral mode does not generate a net anomalous charge in an electric field. However, since the 1D chiral modes that comprise the rank-2 chiral mode with opposite chirality also have opposite transverse momenta, i.e., they have momentum-chirality locking, there will be an anomalous conservation law for the momentum density in the  $i$ -th direction  $\rho_i$ . Specifically, for a uniform system the anomalous conservation law reduces to:

$$\partial_t \begin{pmatrix} \rho_x \\ \rho_y \end{pmatrix} = \chi_2 \frac{e\Lambda^2}{4\pi^2} \begin{pmatrix} E_y \\ E_x \end{pmatrix}, \quad (3)$$

where  $\Lambda$  is a momentum-cutoff scale<sup>1</sup>.

We see from Eq. 3 that a rank-2 mode has an anomalous momentum response to a charge electric field. Remarkably, there is a related inverse effect where an anomalous charge response is produced by a ‘‘momentum’’ electric field. A momentum electric field is generated by a rank-2 tensor gauge field  $\mathbf{e}_\mu^a$  (for the translation symmetry) that couples to the momentum vector charge  $k_a$  instead of the electric charge. Additionally, one can provide an interpretation of the translation gauge fields in terms of elasticity theory where  $\mathbf{e}_\mu^a = \delta_\mu^a - \frac{\partial u^a}{\partial x_\mu}$  where  $u^a$  is the elastic displacement vector. Now, if we consider applying the momentum electric field  $\mathcal{E}_x^y = \partial_x \mathbf{e}_0^y - \partial_t \mathbf{e}_x^y$  we find that modes at  $k_y > 0$  ( $k_y < 0$ ) see an effective electric field in the  $+\hat{x}$  ( $-\hat{x}$ ) direction, and analogously for  $\mathcal{E}_y^x = \partial_x \mathbf{e}_0^x - \partial_t \mathbf{e}_y^x$ . Thus, instead of the canceling effects of an ordinary electric field, in this case the contributions from opposite chiralities add up together. As shown in Ref. 1 this leads to an anomalous conservation law (simplified for a uniform system):

$$\partial_t \rho = \chi_2 \frac{e\Lambda^2}{4\pi^2} (\mathcal{E}_x^y + \mathcal{E}_y^x). \quad (4)$$

To summarize, since for a rank-2 mode opposite momenta have opposite chiralities, but also see opposite effective electric fields in the presence of a momentum electric field  $\mathcal{E}_x^y$  or  $\mathcal{E}_y^x$ , there is an anomalous contribution to the charge density.

To realize a non-zero rank-2 chirality in the long time dynamics of a lattice system, we consider a single-band NH lattice model with Bloch Hamiltonian:

$$H(\mathbf{k}) = \sin k_x \sin k_y + i(\cos k_x + \cos k_y - m), \quad (5)$$

which necessarily has a mirror symmetry along  $x = y$ , and is reciprocal, i.e.,  $H(\mathbf{k}) = H^T(-\mathbf{k})$  where  $H^T$  is the transpose of  $H$ . From the real and imaginary



parts of the energy dispersion of Eq. 5, shown in the top left panel of Fig. 1, it is straightforward to see that the most long-lived mode (mode with largest imaginary energy) near the Fermi energy  $E = 0$  is a rank-2 chiral mode with  $\chi_2 = +1$  around the  $\Gamma$ -point in the Brillouin zone. Since the iso-energy (Fermi surface) contours of the rank-2 mode are open hyperbolas, our construction effectively lets us realize non-closed Fermi lines in a 2D lattice system. The group velocity of the long-lived rank-2 mode around the  $\Gamma$  point is given by  $\mathbf{v} = \partial \text{Re } E(\mathbf{k}) / \partial \mathbf{k} = (k_y, k_x)$ , which suggests that a long-lived state with  $(k_x, k_y)$  will contribute a current along the  $(k_y, k_x)$  direction as illustrated in the bottom right panel of Fig. 1. Similar to the 1D case, since these currents are not compensated at long-times, they are expected to produce accumulated states localized on the edge and/or the corner as depicted in the bottom left panel of Fig. 1. To provide intuition for this expectation let us consider each case: (i) for  $(k_x, k_y) = (0, 0)$  the corresponding state will be extended in the bulk (region I) because its group velocity is zero and thus it does not contribute to a unidirectional current, (ii) for states on the  $k_x$  ( $k_y$ ) axis the velocity is in the  $y$ -direction ( $x$ -direction), hence states will localize on the top/bottom (left/right) edges depending on the sign of the momentum (region II), and (iii) for states off the axes in one of the quadrants the states will localize near the four corners of the square (region III), because they have nonzero group velocity along both directions. Following this picture, in a system with  $N^2$  sites, one expects to observe  $O(1)$  bulk-localized modes,  $O(N)$  edge-localized modes, and  $O(N^2)$  corner-localized modes that correspond to states on points, lines, and areas in momentum space. We emphasize that the rank-2 NHSE inherits the reciprocity of the Hamiltonian, i.e., states with opposite momentum localize on opposite boundaries. This is fundamentally different from the non-reciprocal NHSE associated with rank-1 chirality imbalances, where skin modes can only be found on one boundary (see Ref. 18 for another instance of a reciprocal NHSE).

We experimentally implemented the model in Eq. 5 using a topolelectric circuit composed of passive elements as shown in Fig. 2 – see also Methods. We use the theoretical foundation discussed in Ref. 16 to map the real space hoppings in the reciprocal tight-binding model into a network of resistors, capacitors, and inductors (Fig. 2a,b). Additional details on the topolelectric circuit design can be found along with a brief review in the Supplementary Materials Sec S1. Using this approach, we constructed a circuit network containing  $8 \times 8$  nodes (Fig. 2b,c), whose circuit Laplacian,  $J$ , implements the tight-binding Hamiltonian in Eq. 5, i.e.,  $J \propto -iH$ . In this implementation, the dynamics generated by the Hamiltonian are mapped to a discrete process where we input a voltage and output a current in one step, and then convert the output current to a part of the input voltage for next step using an appropriate impedance normalization factor. Specifically, the input voltage in the  $(n + 1)$ -th step (i.e.,  $V_{n+1}$ ) is generated by the input voltage in the  $n$ -th step (i.e.,  $V_n$ ) through  $V_{n+1} = (1 + \alpha g_n J) V_n$ , where  $\alpha$  is the discrete “time” interval, and  $g_n$  is the normalization factor. To illustrate an example for our circuit network in Fig. 2b,c, we choose  $\alpha = 0.01$  and  $g_n = 1 / \max(JV_n)$  to simulate this discrete process, and we indeed

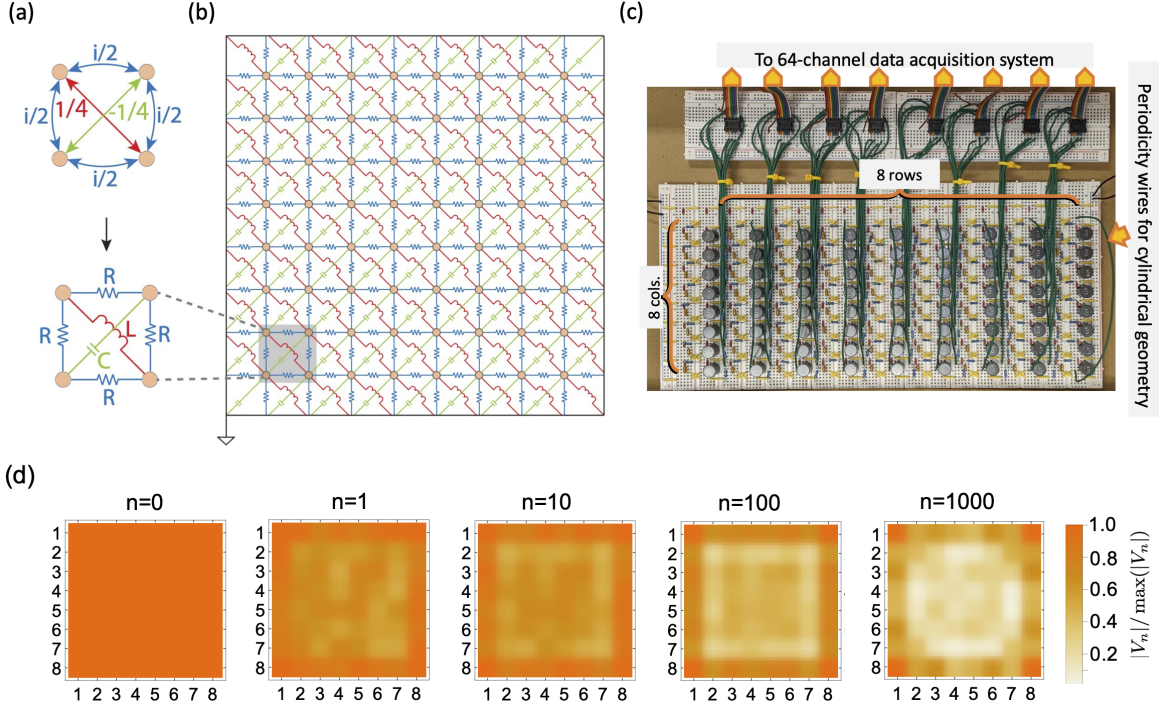


**Figure 2: Implementation of rank-2 chiral dispersion in a topoelectric circuit.** (a) The real space hoppings of the tight-binding model  $H(\mathbf{k}) = \sin k_x \sin k_y + i(\cos k_x + \cos k_y - m)$  [c.f. Eq. 5] and their circuit implementations. Resistors  $R$ , inductors  $L$ , and capacitors  $C$  are selected to satisfy the relationship  $\omega C : \frac{1}{\omega L} : \frac{1}{R} = 1 : 1 : 2$  for a selected frequency (4.95 kHz). (b) Diagram for a 64-node circuit that is an implementation of the tight-binding model in Eq. 5 on a  $8 \times 8$  square lattice. (c) Photograph of the assembled circuit board, of which each row/column corresponds to that in (b) directly. Each node is wired to a 64-channel data acquisition system. (d) Simulation showcasing the dynamical rank-2 behavior in the 64-node circuit network, where  $n$  labels the step and  $V_n$  (indicated by the color scale at each node) is the input voltage in  $n$ -th step.

observe the rank-2 dynamics discussed above, i.e., there are flows toward the edges and corners as shown in Fig. 2d.

For our measurements we first configure the topoelectric circuit in a cylindrical geometry, that is, with a periodic boundary condition along  $x$ , and an open boundary along  $y$  as shown in Fig. 3a. This is easily achieved with the help of appropriate wiring in the circuit. We measure the cross-impedance matrix  $G_{ab} = V_a^{\text{output}}/I_b^{\text{input}}$  where  $V_a^{\text{output}}$  is the voltage at any node  $a$  in response to input current  $I_b^{\text{input}}$  at any node  $b$ . This matrix  $G$  is the inverse of the circuit Laplacian and therefore has the same eigenvectors. We can diagonalize  $G$  to examine the eigenvectors of the circuit Laplacian. When we visualize the eigenstates of  $G$ , the NHSE is readily observed as an extensive number of eigenstates localized on the open boundaries. In the Supplemental Material Sec S2 we discuss how the phase information encoded in the eigenstates can be used

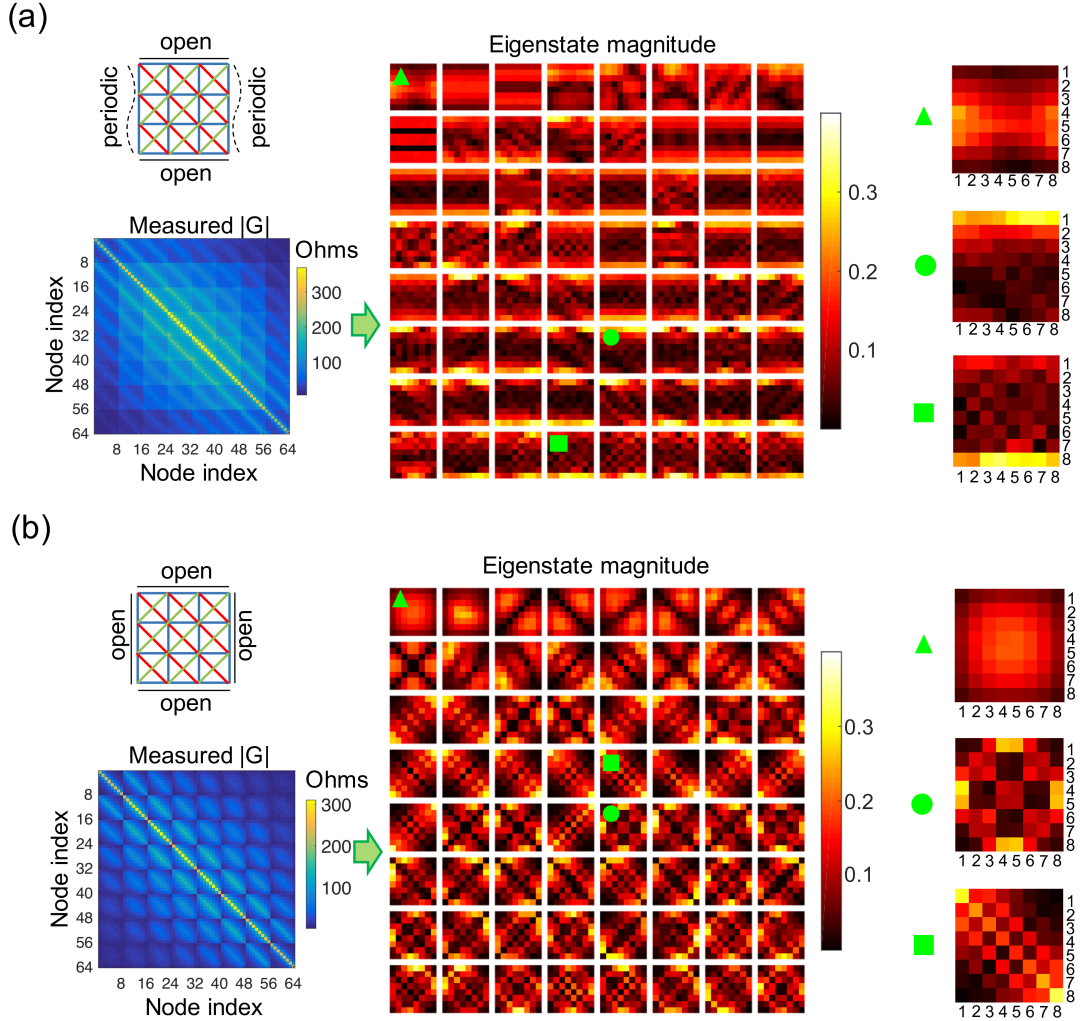


**Figure 3: Measurements of cross-impedance matrix  $G$  and its eigenstates under cylinder and square geometries.** (a) Visualization of the magnitude of measured matrix  $G$  (phase not presented) and its eigenstates under a cylinder geometry, where  $x$  direction is periodic but  $y$  direction is open as shown in the top left panel. The lines with different colors in the top left panels correspond to different hoppings previously shown in Fig.2. Some representative bulk, top-edge, and bottom-edge localized eigenstates are zoomed in on the right. (b) The measured matrix  $G$  and its eigenstates under a square geometry, where both  $x$  and  $y$  directions are open as shown in the top left panel. Some representative bulk, edge, and corner corner modes are zoomed in on the right.

to confirm that this NHSE is momentum resolved.

To further observe the rank-2 phenomenology we configured the material with a square geometry where both the  $x$  and  $y$ -directions are open. The measured  $G$  matrix and its eigenstates are visualized in Fig. 3b. As expected from

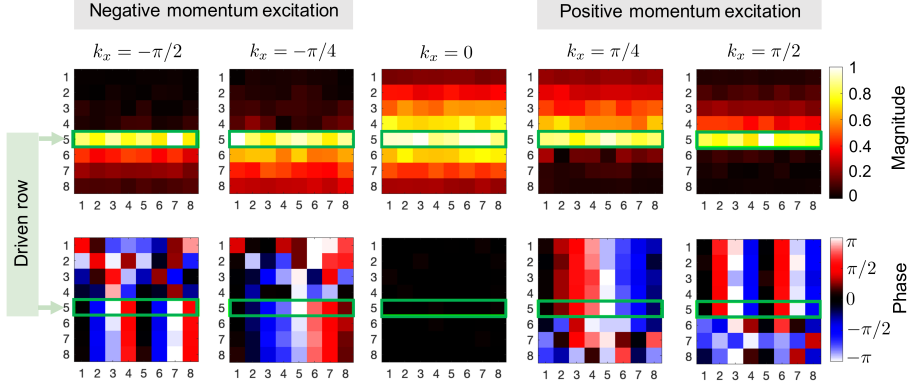


**Figure 4: Responses to input excitations for the cylinder geometry.** We apply voltage inputs on the fifth row (highlighted by the green box) with relative phase corresponding to momentum  $k_x$ . The specific momentum values are quantized by the periodicity and number of nodes in the structure. The top and bottom figures are paired and show the magnitudes and phase (relative to node driven with phase 0) of the output voltages for each case.

the intuitive picture (Fig. 1), we find the eigenstates localized in the bulk, edges, and corners of the system. A shortcoming of the intuitive picture in Fig. 1 is that it only considers states in a small energy/momentum window around  $k_x = k_y = 0$ , hence we cannot derive an exact counting rule for bulk-, edge-, and corner-localized modes for a finite open system. Even so, we observe that the order of the number of modes matches well with the expectations: there are  $O(1)$  bulk-localized modes corresponding to states with group velocity  $v_x = v_y = 0$ ,  $O(N)$  edge-localized modes arising from states with group velocity  $v_x \neq 0, v_y = 0$  and  $v_x = 0, v_y \neq 0$ , and  $O(N^2)$  corner-localized modes arising from states having group velocity  $v_x, v_y \neq 0$  (where  $N=8$  for our system).

Another key feature related to the rank-2 NHSE is that the momentum-chirality locking is converted to momentum-location locking (i.e., to edges and corners in the context of the rank-2 NHSE) in response to input excitations. To see this effect, we can experimentally apply voltage signals with relative phase differences that will introduce excitations with defined momenta (we note that the applied relative phase difference directly corresponds to the momentum in units of radians per node). In Fig. 4 we show the response for the cylindrical geometry configuration by exciting a row of the circuit with a nonzero  $x$ -directed momentum  $k_x$ . The measured output voltages explicitly show the momentum-location locking, i.e., as seen in Fig. 4, voltage inputs with positive (negative) momentum  $k_x$  lead to a voltage accumulation on the top (bottom) edge. The relative phase measured between adjacent nodes along the respective edges matches the input signals, confirming the same  $k_x$  momentum associated with the localized input. We also remark that the special case of  $k_x = 0$  leads to only a symmetric voltage response around the excited row, i.e. it does not exhibit a preferred locking effect as is expected from our theory analysis. These

observed responses to input voltages directly indicate a unidirectional momentum flow in an infinite system with nonzero rank-2 chirality, i.e., excitations with opposite momenta flow in opposite directions.

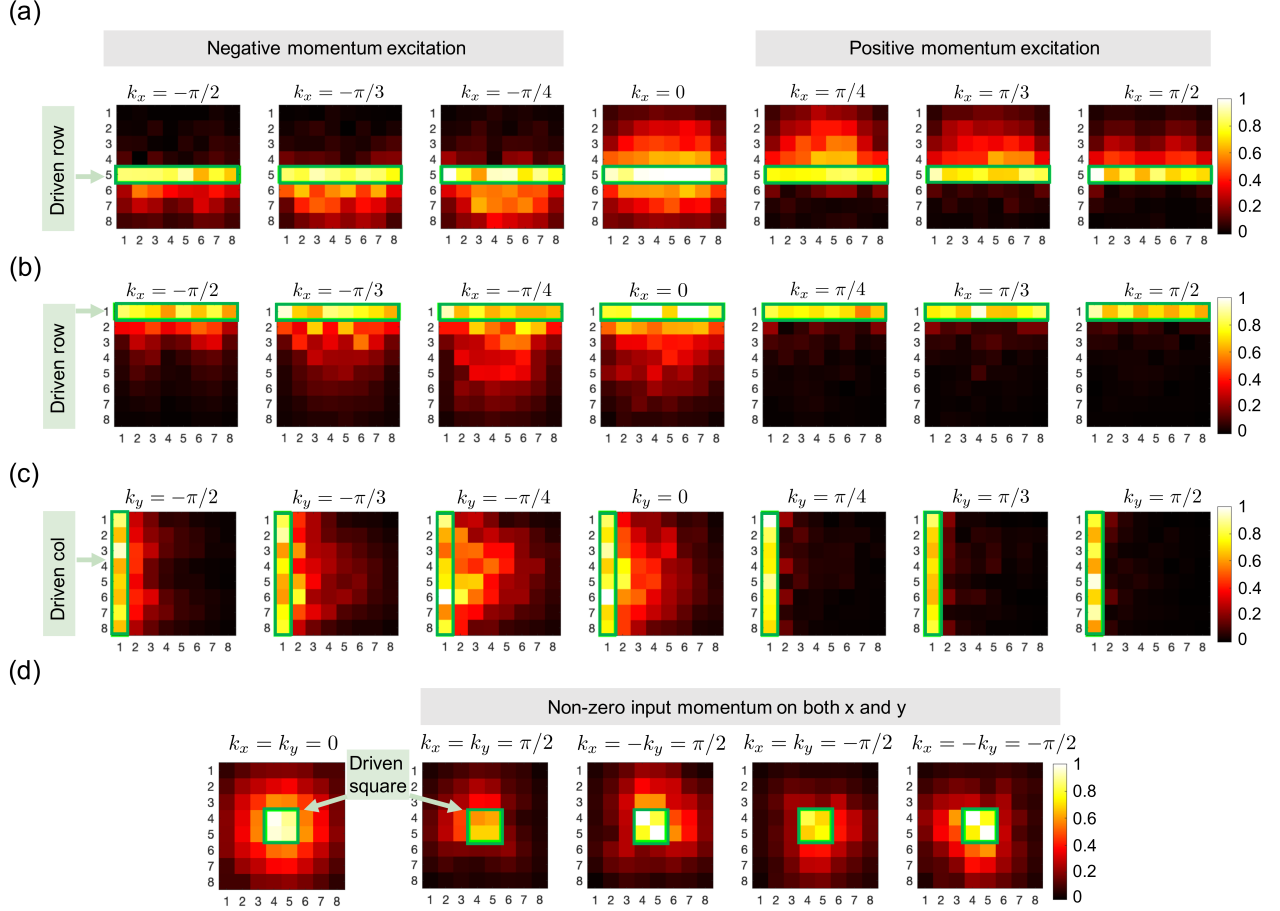


**Figure 5: Responses to input excitations for the square geometry.** The magnitude of voltage responses to different  $k_x$  input on (a) the fifth row and (b) the first row are presented. (c) Similarly shows the magnitude of voltage responses to different  $k_y$  input on the first column. (d) The magnitude of voltage responses to simultaneous  $(k_x, k_y)$  input on the central square showing the corner-directed responses. Complete data sets including phase information are presented in the Supplementary Material Sec. S4.

We next open both boundaries, as one would find in a, perhaps more practical, finite material (as configured in Fig. 2b). Even though the system is finite and momenta are not well defined, we can still consider the relative excitation phase as a proxy for  $x$  and  $y$  momenta  $k_x$  or  $k_y$ . Results from various excitations are presented in Fig. 5. When applying excitations purely along  $x$  or  $y$  (Fig. 5a-c) we can confirm that the momentum-location locking effect persists.

As a curious aside, we surprisingly find that even though the voltage inputs with  $\pm k_x$  or  $\pm k_y$  on the boundary row or column lead to quite different configurations of output voltages (see Fig. 5b-c where we see some responses are extended into the bulk while some are extremely localized on the boundary), the effective load experienced by the excitation source is purely real and symmetric with respect to  $k_x$  or  $k_y$ . Interested readers are referred to the Supplementary Material Sec S3 for more details.

More interestingly, if we input signals having non-zero momentum simultaneously along both  $x$  and  $y$  directions we can see a voltage accumulation toward the corners as shown in Fig. 5d. This result once more verifies the intuitive picture about rank-2 NHSE. While we only present the amplitude responses here, the complete picture including the corresponding phase response can be found in Supplementary Material Sec S4.

In this combined theoretical and experimental study, we have presented the first 2D material that exhibits higher-rank chiral behavior. We specifically study both the rank-2 NHSE, as well as the remarkable momentum-resolved response that causes excitations in a finite system to lock to edges and corners. The responses observed in Fig. 4 and Fig. 5 directly confirm that the sign of group velocity of modes with momentum  $(k_x, k_y)$  is given by  $(\text{sgn}(k_y), \text{sgn}(k_x))$ , and thus probes the rank-2 chirality. Since the rank-2 chirality determines the anomalous momentum and particle currents<sup>1</sup>, the observed responses to input voltage signals can also be understood as an indirect probe of the charge and momentum anomalies due to a nonzero rank-2 chirality.

Looking forward, our circuit-based approach shows the potential for exploration of chiral physics in higher dimensions, including the unusual responses to externally applied electromagnetic and geometric fields. Notably, the ability to resolve vector momentum is particularly important in practical beamforming and sensor applications. While the effects we show here are entirely reciprocal, the highly asymmetric momentum-resolved responses are also a key ingredient for producing non-reciprocal metamaterials.

## Methods

**Circuit construction:** The specific component values used for the topoelectric circuit implementation were  $L = 47$  mH ( $\pm 5\%$ ),  $C = 22$  nF ( $\pm 1\%$ ), and  $R = 732$  ohm ( $\pm 1\%$ ). This allows the circuit Laplacian to model the desired Hamiltonian at approximately 4.95 kHz. All components were assembled on solderless prototyping breadboards. **Data acquisition:** Experimental measurements were performed using Matlab and its built-in data acquisition toolbox. For cross-impedance matrix characterization, the drive currents were generated using a bench-top signal generator set to 4.95 kHz, sending its voltage output through a 497 ohm reference resistor. For the driven response tests, the phase-synchronized signals were generated using a National Instruments NI 9264 volt-

age output module. All response signals were captured using Keysight U2331A (64-channel) data acquisition hardware, with each channel set to one node of the 8x8 array. The magnitude and phase responses were measured against the drive signals using a digital lock-in that we coded in Matlab.

## References

- [1] Dubinkin, O., Burnell, F. & Hughes, T. L. Higher rank chiral fermions in 3d weyl semimetals. *arXiv preprint arXiv:2102.08959* (2021).
- [2] Nielsen, H. B. & Ninomiya, M. Absence of neutrinos on a lattice:(i). proof by homotopy theory. *Nuclear Physics B* **185**, 20–40 (1981).
- [3] Nielsen, H. B. & Ninomiya, M. Absence of neutrinos on a lattice:(ii). intuitive topological proof. *Nuclear Physics B* **193**, 173–194 (1981).
- [4] Qi, X.-L. & Zhang, S.-C. Topological insulators and superconductors. *Rev. Mod. Phys.* **83**, 1057–1110 (2011).
- [5] Sun, X.-Q., Xiao, M., Bzdušek, T., Zhang, S.-C. & Fan, S. Three-Dimensional Chiral Lattice Fermion in Floquet Systems. *Phys. Rev. Lett.* **121**, 196401 (2018).
- [6] Lee, J. Y., Ahn, J., Zhou, H. & Vishwanath, A. Topological correspondence between hermitian and non-hermitian systems: Anomalous dynamics. *Phys. Rev. Lett.* **123**, 206404 (2019).
- [7] Song, F., Yao, S. & Wang, Z. Non-hermitian skin effect and chiral damping in open quantum systems. *Phys. Rev. Lett.* **123**, 170401 (2019).
- [8] Bessho, T. & Sato, M. Nielsen-ninomiya theorem with bulk topology: Duality in floquet and non-hermitian systems. *Phys. Rev. Lett.* **127**, 196404 (2021).
- [9] Weidemann, S. *et al.* Topological funneling of light. *Science* **368**, 311–314 (2020).
- [10] Hu, B. *et al.* Non-hermitian topological whispering gallery. *Nature* **597**, 655–659 (2021).
- [11] Hatano, N. & Nelson, D. R. Localization transitions in non-hermitian quantum mechanics. *Phys. Rev. Lett.* **77**, 570–573 (1996).
- [12] Yao, S. & Wang, Z. Edge states and topological invariants of non-hermitian systems. *Phys. Rev. Lett.* **121**, 086803 (2018).
- [13] Lee, C. H. & Thomale, R. Anatomy of skin modes and topology in non-hermitian systems. *Phys. Rev. B* **99**, 201103 (2019).

- [14] Okuma, N., Kawabata, K., Shiozaki, K. & Sato, M. Topological origin of non-hermitian skin effects. *Phys. Rev. Lett.* **124**, 086801 (2020).
- [15] Zhang, K., Yang, Z. & Fang, C. Correspondence between winding numbers and skin modes in non-hermitian systems. *Phys. Rev. Lett.* **125**, 126402 (2020).
- [16] Lee, C. H. *et al.* Topoelectrical circuits. *Communications Physics* **1**, 1–9 (2018).
- [17] Peskin, M. E. & Schroeder, D. V. *An Introduction to quantum field theory* (Addison-Wesley, Reading, USA, 1995).
- [18] Hofmann, T. *et al.* Reciprocal skin effect and its realization in a topoelectrical circuit. *Phys. Rev. Research* **2**, 023265 (2020).

## Acknowledgments

This work was sponsored by the Multidisciplinary University Research Initiative (MURI) grant N00014-20-1-2325 and the US National Science Foundation EFRI grant EFMA-1641084. X.-Q.S. acknowledges support from the Gordon and Betty Moore Foundation’s EPiQS Initiative through Grant GBMF8691. G.B. would additionally like to acknowledge support from the Office of Naval Research (ONR) Director for Research Early Career grant N00014-17-1-2209, and the Presidential Early Career Award for Scientists and Engineers. The authors thank Sasha Yamada for assistance with data acquisition.

## Author contributions

P.Z. and X.-Q.S. performed the theoretical study. P.Z. and G.B. designed the experiments. G.B. performed the experimental study. T.L.H. and G.B. supervised the work. All authors jointly wrote the paper.

## Data availability

The data that support the findings of this study are available from the corresponding author upon reasonable request.

## Code availability

The codes that support the findings of this study are available from the corresponding author upon reasonable request.



# Supplementary Materials: Higher rank chirality and momentum resolved non-Hermitian skin effect in a topoelectrical circuit

Penghao Zhu<sup>1</sup>, Xiao-Qi Sun<sup>1</sup>,  
Taylor L. Hughes<sup>1</sup>, and Gaurav Bahl<sup>2</sup>

<sup>1</sup>Department of Physics and Institute for Condensed Matter Theory,

<sup>2</sup>Department of Mechanical Science and Engineering,

University of Illinois at Urbana-Champaign, Urbana, IL 61801, USA

## S1 Review of topoelectric circuit theory

We present here a brief review of the theoretical foundation for topoelectric circuits, based on the extensive discussion that can be found in Ref. 16. The behavior of any passive circuit with only resistors, capacitors, and inductors is governed completely by Kirchhoff's and Ohm's laws. The total input current into a node equals the total outgoing current from that node:

$$I_a = \sum_j I_{aj} + I_{aG}, \quad (\text{S1})$$

where  $I_a$  is the total input current into node  $a$ , and  $I_{aj}$  is the current flowing from node  $a$  to an adjacent (directly connected) node  $j$ , and  $I_{aG}$  is the current flowing from node  $a$  to the ground. The relation between the currents and voltages in the network is:

$$\dot{I}_{aj} = C_{aj} (\ddot{V}_a - \ddot{V}_j) + \frac{1}{R_{aj}} (\dot{V}_a - \dot{V}_j) + \frac{1}{L_{aj}} (V_a - V_j), \quad (\text{S2})$$

where the dot indicates a time derivative;  $V_i$  is the voltage of node  $i$ ;  $C_{aj}$ ,  $R_{aj}$ , and  $L_{aj}$  are capacitors, resistors, and inductors between node  $a$  and node  $j$ . If we Fourier transform Eq. S1 and Eq. S2, we obtain two frequency-dependent equations:

$$\begin{aligned} I_a(\omega) &= \sum_j I_{aj}(\omega) + I_{aG}(\omega), \\ I_{aj}(\omega) &= \left( i\omega C_{aj} + \frac{1}{R_{aj}} + \frac{1}{i\omega L_{aj}} \right) (V_a(\omega) - V_j(\omega)), \end{aligned} \quad (\text{S3})$$

where  $\omega$  is the angular frequency. From Eq. S3, we can write the relation between the input currents and output voltages as

$$I_a(\omega) = J_{ab} V_b(\omega), \quad (\text{S4})$$

where  $I = (I_1 \ I_2 \ \dots)^T$ ,  $V = (V_1 \ V_2 \ \dots)^T$ , and  $J$  is the circuit Laplacian matrix with entries

$$\begin{aligned} J_{aj} &= -\left(i\omega C_{aj} + \frac{1}{R_{aj}} + \frac{1}{i\omega L_{aj}}\right) \\ J_{aa} &= \left(i\omega C_{aG} + \frac{1}{R_{aG}} + \frac{1}{i\omega L_{aG}}\right) + \sum_{j \neq a} \left(i\omega C_{aj} + \frac{1}{R_{aj}} + \frac{1}{i\omega L_{aj}}\right), \end{aligned} \quad (\text{S5})$$

where  $C_{aG}$ ,  $R_{aG}$ , and  $L_{aG}$  are capacitors, resistors, and inductors between node  $a$  and the ground. By construction,  $J$  is a symmetric matrix.

The core idea behind topoletric circuits is to realize a tight-binding Hamiltonian using the circuit Laplacian. In other words, given a symmetric tight-binding Hamiltonian  $H$  in real space (or equivalently a reciprocal Hamiltonian in momentum space, i.e.,  $H(\mathbf{k}) = H^T(-\mathbf{k})$ ), we can find a circuit Laplacian  $J$  such that  $H = iJ$ , and  $J_{aj}$  can be identified as the real space hoppings between sites  $a$  and sites  $j$  in the Hamiltonian  $H$ . If we want to find a topoletric circuit realization of a non-symmetric  $H$ , then we need to include more components besides resistors, capacitors, and inductors.

Using the general theory reviewed above, we can identify the corresponding circuit Laplacian for Hamiltonian  $H(\mathbf{k}) = \sin k_x \sin k_y + i(\cos k_x + \cos k_y - m)$  in Eq. 5. We first Fourier transform the Bloch Hamiltonian into real space to get the real space hoppings plotted in Fig. 2a :

$$\begin{aligned} H &= \sum_{x,y} -\frac{1}{4}c_{x,y}^\dagger c_{x+1,y+1} + \frac{1}{4}c_{x,y+1}^\dagger c_{x+1,y} + h.c. \\ &+ i \sum_{x,y} \frac{1}{2}c_{x+1,y}^\dagger c_{x,y} + \frac{1}{2}c_{x,y+1}^\dagger c_{x,y} + h.c., \end{aligned} \quad (\text{S6})$$

We want to design a circuit such that its Laplacian satisfies  $J = -isH$ , where  $s$  is a scale factor. As shown in Fig. 2a, we use capacitors  $C$  and inductors  $L$  to realize the two digonal hoppings with opposite sign, and use resistors  $R$  to realize hoppings along  $x$  and  $y$  directions, and the  $R$ ,  $L$ , and  $C$  are selected to satisfy  $\omega C : \frac{1}{\omega L} : \frac{1}{R} = 1 : 1 : 2$  for a selected frequency (4.95 kHz).

## S2 Momentum information encoded in the edge-localized modes

In Fig. S1 we take a closer look at the phase information associated with the two eigenstates localized on opposite boundaries (labeled with the green disk and square in Fig. 3a). We observe that the adjacent nodes on the top (or bottom) edge have a very clear and consistent relative phase difference of  $\delta\phi = \pi/2$  (or  $\delta\phi = -\pi/2$ ). This can be interpreted as momentum  $k_x = \pi/2$  (or  $k_x = -\pi/2$ ). A similar analysis can be readily performed on the other eigenmodes (not presented for brevity) to confirm that modes with opposite momentum localize on opposite edges, which is the expected momentum resolved NHSE.

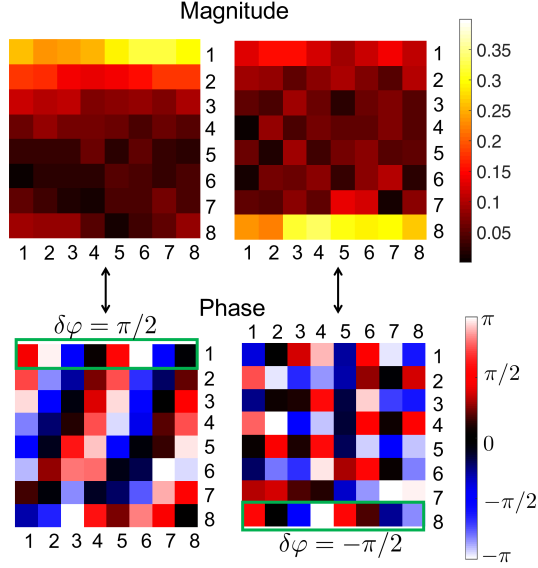


**Figure S1: Magnitude and phase of edge-localized eigenstates.** The top and bottom rows show the magnitude and phase for the two representative edge-localized eigenstates identified in Fig. 3a. The value of  $\delta\phi$  for the rows highlighted in green indicates the relative phase difference between the  $n + 1$ -th and  $n$ -th nodes on the boundary.

### S3 Effective local impedance of the circuit with respect to excitations with different momenta

Let us consider a cylindrical geometry where the  $x$ -direction is periodic and  $y$ -direction is open. We can perform an explicit circuit analysis to show that the effective local impedances experienced by excitations on the open edge row are identical with respect to  $\pm k_x$  excitations (assuming a semi-infinite circuit). To do this, we solve for the current response to an applied voltage input with frequency  $\omega$  with momentum  $k_x$  on the open edge row. Because of translation symmetry along  $x$ -direction, the effective local impedance of nodes within any row will be identical, and so we only need to focus on one column and its neighbors (see Fig. S2a).

From Kirchhoff's and Ohm's laws we have the relation:

$$I_2 = \frac{V_2 - V_1}{R} + \frac{V_2 - V_3}{R} + \frac{V_2 - V_5}{R} + \frac{V_2}{R} + V_2(i\omega C + \frac{1}{i\omega L}) + i\omega C(V_2 - V_4) + \frac{V_2 - V_6}{i\omega L}, \quad (S7)$$

where  $V_j$  is the voltage of node  $j$ , and  $I_j$  is the net current flow into node  $j$ , for excitation at frequency  $\omega$ . Note that in our system  $i\omega C + 1/(i\omega L) = 0$  and  $2\omega C = 2/(\omega L) = 1/R$  at the frequency of interest. If we have a plane wave

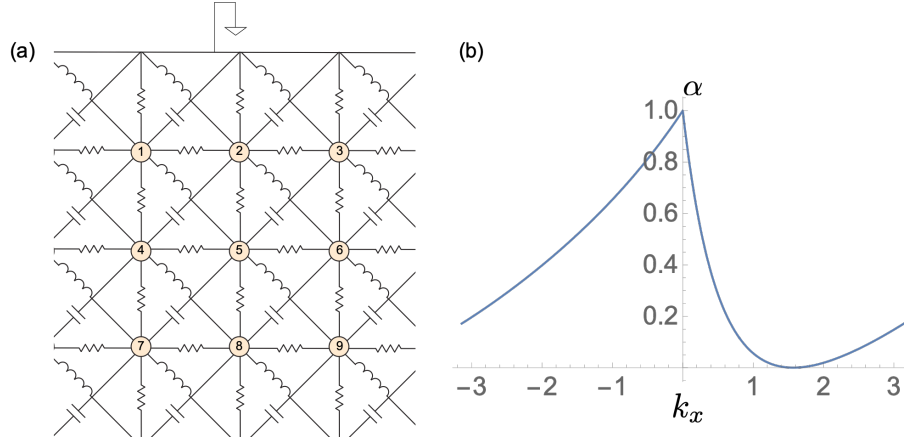


**Figure S2: Circuit analysis of response to a boundary voltage input.** (a) A part of our circuit used in the circuit analysis. (b) The ratio between voltage magnitude between the  $j$ -th row and  $(j+1)$ -th row.

voltage (i.e.,  $V_{1n} = \exp(ik_x n)$ ) input on the first row, given the translation symmetry along  $x$  direction, the voltage on the  $j$ -th row should also take the form  $V_{jn} = A_j \exp(ik_x n)$ . Then, the above equation becomes

$$\begin{aligned}
 I_2 &= V_2 \left( \frac{4}{R} - \frac{1}{R} \exp(-ik_x) - \frac{1}{R} \exp(ik_x) - \frac{1}{R} \frac{V_5}{V_2} - i\omega C \frac{V_4}{V_2} - \frac{1}{i\omega L} \frac{V_6}{V_2} \right) \\
 &= V_2 \left( \frac{4}{R} - \frac{2}{R} \cos k_x - \frac{\alpha_1}{R} - i\omega C \alpha_1 e^{-ik_x} - \frac{\alpha_1 e^{ik_x}}{i\omega L} \right) \\
 &= V_2 \left( \frac{4}{R} - \frac{2}{R} \cos k_x - \frac{\alpha_1}{R} - \alpha_1 \left( \omega C + \frac{1}{\omega L} \right) \sin k_x \right) \\
 &= V_2 \left( \frac{4}{R} - \frac{2}{R} \cos k_x - \frac{\alpha_1}{R} (1 + \sin k_x) \right),
 \end{aligned} \tag{S8}$$

where  $\alpha_1 = A_2/A_1$ . Thus, the effective local impedance is

$$Z = \frac{V_2}{I_2} = \frac{R}{4 - 2 \cos k_x - \alpha_1 (1 + \sin k_x)}, \tag{S9}$$

where  $\alpha_1 \equiv \alpha_1(k_x)$ . More generally, we define  $\alpha_n = A_{n+1}/A_n$ . Let us now

calculate  $\alpha_n$ .

$$\begin{aligned}
I_5 &= 0 \\
&= \frac{V_5 - V_2}{R} + \frac{V_5 - V_4}{R} + \frac{V_5 - V_6}{R} + \frac{V_5 - V_8}{R} + \frac{V_5 - V_1 + V_5 - V_9}{i\omega L} \\
&\quad + i\omega C(V_5 - V_3 + V_5 - V_7) \\
&= V_5 \left( \frac{4}{R} - \frac{1}{\alpha_1 R} - \frac{2}{R} \cos k_x - \frac{\alpha_2}{R} - \frac{\frac{1}{\alpha_1} e^{-ik_x} + \alpha_2 e^{ik_x}}{i\omega L} \right. \\
&\quad \left. - i\omega C \left( \frac{1}{\alpha_1} e^{ik_x} + \alpha_2 e^{-ik_x} \right) \right) \\
&= V_5 \left( \frac{4}{R} - \frac{1}{\alpha_1 R} - \frac{2}{R} \cos k_x - \frac{\alpha_2}{R} - \frac{-i\frac{1}{\alpha_1} \sin k_x + i\alpha_2 \sin k_x}{i\omega L} \right. \\
&\quad \left. - i\omega C \left( i\frac{1}{\alpha_1} \sin k_x - i\alpha_2 \sin k_x \right) \right) \\
&= V_5 \left( \frac{4}{R} - \frac{1}{\alpha_1 R} - \frac{2}{R} \cos k_x - \frac{\alpha_2}{R} + \frac{1}{\alpha_1} \left( \frac{1}{\omega L} + \omega C \right) \sin k_x \right. \\
&\quad \left. - \alpha_2 \left( \frac{1}{\omega L} + \omega C \right) \sin k_x \right), \tag{S10}
\end{aligned}$$

which indicates that

$$4 - 2 \cos k_x - \frac{1}{\alpha_1} (1 - \sin k_x) - \alpha_2 (1 + \sin k_x) = 0. \tag{S11}$$

Since our circuit also has a translation symmetry along  $y$ -direction, the above equation is true for any  $\alpha_n$  and  $\alpha_{n+1}$ :

$$4 - 2 \cos k_x - \frac{1}{\alpha_n} (1 - \sin k_x) - \alpha_{n+1} (1 + \sin k_x) = 0. \tag{S12}$$

In a semi-infinite geometry, we have all  $\alpha_n$  equal to  $\alpha$ , because of the translation symmetry along the  $y$ -direction. Thus the above equation becomes

$$\alpha^2 (1 + \sin k_x) - \alpha (4 - 2 \cos k_x) + (1 - \sin k_x) = 0, \tag{S13}$$

from which we can solve

$$\alpha_{\pm} = \frac{2 - \cos k_x \pm 2\sqrt{1 - \cos k_x}}{(1 + \sin k_x)}. \tag{S14}$$

We note that we should choose  $\alpha_-$  because when  $k_x = \pi/2$ , we expect  $\alpha$  to be less than one, thus the  $\alpha_-$  solution physically makes sense. Finally we get

$$\alpha(k_x) = \frac{2 - \cos k_x - 2\sqrt{1 - \cos k_x}}{(1 + \sin k_x)}, \tag{S15}$$

which is plotted in Fig. S2b. Note that the singular point at  $k_x = -\pi/2$  is removable in the sense that  $\lim_{k_x \rightarrow -\pi/2} \alpha(k_x) = 1/2$ .

From Fig. S2b, we clearly see  $\alpha$  is asymmetric for  $\pm k_x$ , which manifests the momentum resolved skin effect. However, if we substitute  $\alpha_1 = \alpha$  into Eq. S9, we get

$$Z = \frac{R}{2 - \cos k_x + 2\sqrt{1 - \cos k_x}}, \quad (\text{S16})$$

which is symmetric with  $k_x$ . In other words, even though the excitation patterns are clearly unequal, the effective impedances are identical irrespective of the directionality of momentum  $\pm k_x$ .

A similar proof can also be applied to evaluate the effective local impedance where there are excitations on a boundary column.

## S4 Complete response measurements under a square geometry

In the main text Fig. 5a-d, we only present the magnitude response to excitations with different  $k_x$  or  $k_y$ . In the figures below we present the complete response measurements including the relative phase information between all the nodes of the circuits.

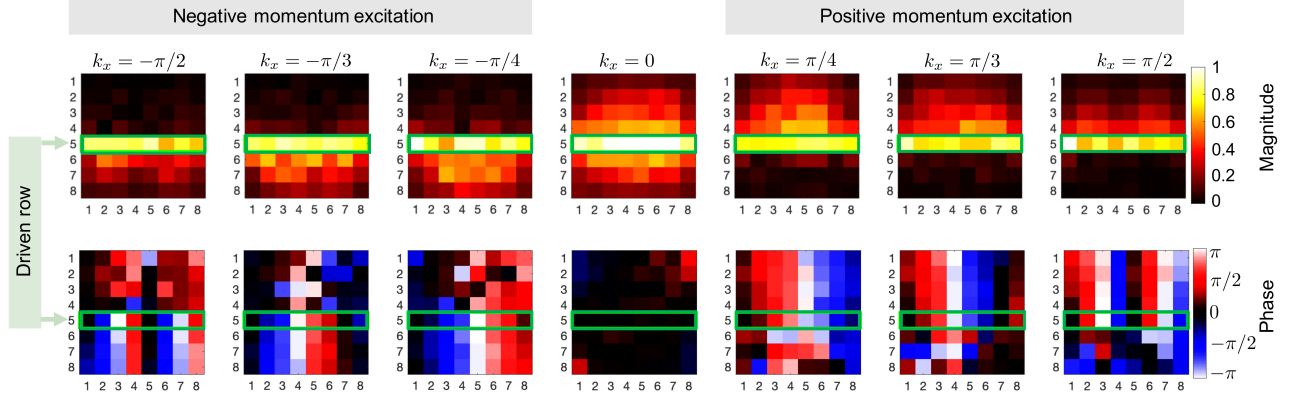


**Figure S3: Responses to input excitations for the square geometry.** Complete measurements of responses including both magnitude and phase information corresponding to Fig. 5a

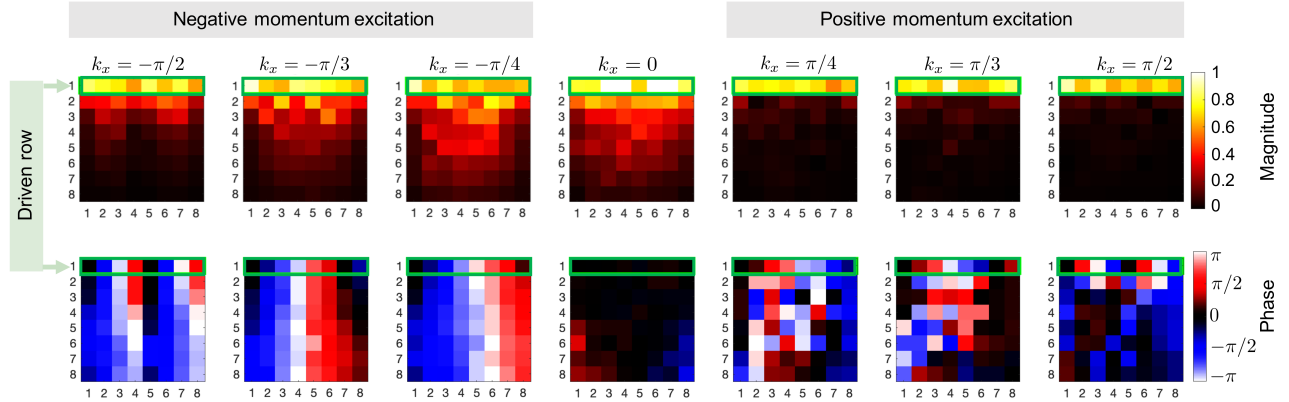


**Figure S4: Responses to input excitations for the square geometry.** Complete measurements of responses including both magnitude and phase information corresponding to Fig. 5b

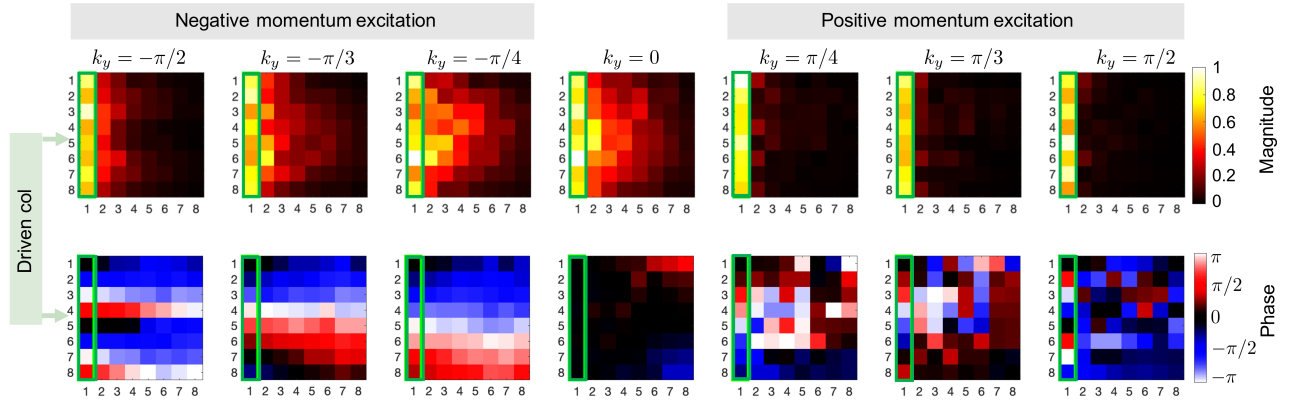


**Figure S5: Responses to input excitations for the square geometry.** Complete measurements of responses including both magnitude and phase information corresponding to Fig. 5c

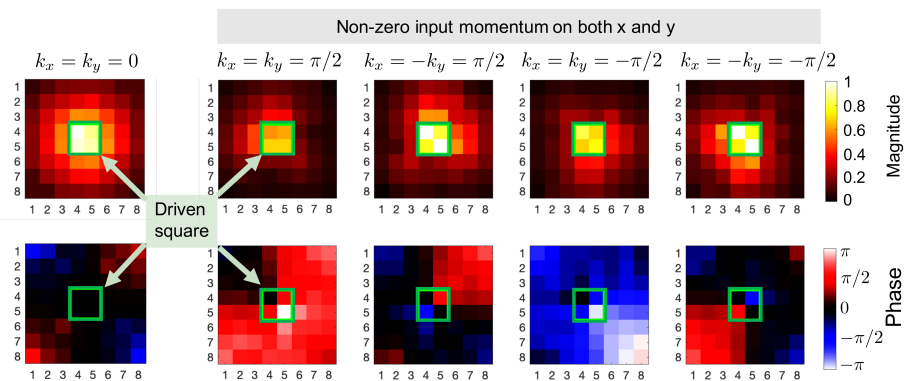


**Figure S6: Responses to input excitations for the square geometry.** Complete measurements of responses including both magnitude and phase information corresponding to Fig. 5d